Received: 27 April 2025 | Revised: 11 June 2025 | Accepted: 26 June 2025 | Published online: 3 July 2025

RESEARCH ARTICLE

Smart Wearable Technology
2025, Vol. 1, A7, 1–12 Pages
DOI: 10.47852/bonviewSWT52026022

Synchronized Measurement of Electromechanical Responses of Fabric Strain Sensors Under Large Deformation

Bao Yang[1], Xianyu Zhu[1], Chang Peng[1], Licheng Zhou[1], Fei Wang[2,*], Zejia Liu[1,*], Liqun Tang[1], Zhenyu Jiang[1], Yiping Liu[1] and Senxin Chen[1]

[1]*School of Civil Engineering and Transportation, South China University of Technology, China*

[2]*School of Textile Science and Engineering, Wuyi University, China*

Abstract: Fabric-based strain sensors hold significant potential across various applications, including sports, healthcare, rehabilitation, etc. Nonetheless, their complex performance under large deformation and varying loading rates, arising from material viscoelasticity and textile structure intricacies, remains inadequately understood. The primary constraint in evaluating their performance lies in the absence of electromechanically coupled instrumentation. This paper endeavors to overcome the limitation by developing a synchronized measurement system, which integrates mechanically controlled loading, voltage divider circuits, and visual measurement technologies. This system enables synchronized acquisition of mechanical and electrical signals spanning from 0.01 mm/min to 6 m/s, by employing material testing machines for low-speed loading and split Hopkinson pressure bars for medium-to-high-speed loading, and combining electrical performance measurements with displacement and strain field analyses. Experiments revealed that sensor sensitivity increased linearly with the logarithm of loading rates, while deformation patterns evolved with loading speed, thereby offering valuable insights into design and calibration of fabric-based strain sensors under dynamic conditions.

Keywords: synchronized measurement, fabric strain sensor, electromechanical behavior, dynamic loading, large deformation

1. Introduction

Smart wearable devices are increasingly integrated into daily life, with every component—materials and substrates, sensors and interconnects, power sources, and system integration—being important [1, 2]. Among these, strain sensors for human motion capture entail both strain sensitivity and wear comfort [3]. Fabric strain sensors (FSS) have garnered attention for their comfort, breathability, large deformability, seamless clothing integration, and high sensitivity [4]. FSSs are pivotal candidates in human motion monitoring and training assistance [5, 6], medical care and rehabilitation [7–9], soft robotic skins [10], and human-machine interaction [11–13].

Human body deformation rates vary significantly across regions and activities. For instance, chest/abdominal skin deformation during breathing is ~ 0.01 m/s [14], while walking speeds range from 0.5 to 1.7 m/s [15]. Tai Chi elbow movements can exceed 4 m/s [16], and a boxer's punch ranges from 4 to 25 m/s [17]. Volleyball/soccer hitting speeds reach 30 m/s [18]. The above motion durations can be as short as 10^{-2} s. Measuring joint skin strain during such motions requires FSS to accommodate strain velocities up to 30 m/s, necessitating research into loading rate effects on sensor performance.

Accordingly, to assess FSS performance under varying movement speeds, quasi-static-dynamic tensile experiments are essential. Quasi-static assessment can be conducted on a universal testing machine, while dynamic tests typically employ drop hammer method, split Hopkinson pressure bars (SHPBs), etc. For example, Wang et al. [19] designed a yarn tensile system combining a universal testing machine (quasi-static) and a drop hammer with loading speed of up to 20 m/s or higher. Similarly, Wang et al. [20] measured the dynamic of FSS embedded in pressure units based on a drop hammer. However, the drop hammer's prolonged acceleration and gravity effects preclude high-speed constant loading. In comparison, SHPBs, which feature a high strain rate ranging from dozens to thousands per second, serve as a powerful tool for studying the dynamic properties of FSS. However, unfortunately, they have rarely been fully utilized in the FSS research field.

Flexible sensors made from graphene, carbon fiber, nano-composite grid materials, and silicone exhibit strain rate sensitivity [21]. Brown et al. [22] and Todo et al. [23] found strain rates affect fabric tensile strength. Wang et al. [20] developed a theoretical model of strain rate on the FSS electromechanical performance, which was established on the basis of generalized Maxwell model. Further, they successfully applied the theoretical model in the study of dynamic impact loading of FSS at strain rate high up to 100/s.

---

[*]**Corresponding authors:** Fei Wang, School of Textile Science and Engineering, Wuyi University, China. Email: 11902640R@connect.polyu.hk and Zejia Liu, School of Civil Engineering and Transportation, South China University of Technology, China. Email: zejialiu@scut.edu.cn

However, research on FSS dynamic electromechanical behavior still lags far behind their quasi-static counterparts. This research disparity results in flexible sensors exhibiting inadequate mechanical robustness during prolonged usage, high-speed loading, and under large deformation [24]. Consequently, the accuracy of these sensors under high-strain and high-impact scenarios is severely compromised. Gaining a comprehensive understanding of the performance characteristics of FSSs under varying strain rates not only has the potential to improve the accuracy of motion monitoring systems but also aligns with the end-to-end design philosophy, which emphasizes holistic optimization from input to output [25].

This paper proposes a Hopkinson rod and Instron-based synchronized experimental method combining dynamic stretching force-electrical performance measurement with digital image correlation (DIC) to study FSS electromechanical behavior from quasi-static to dynamic stretching. By measuring parameters under different loading rates, it explores strain rate effects on FSS performance, aiming to improve human motion measurement accuracy at varied speeds.

2. Evaluation System

To examine the electromechanical performance of FSS under conditions ranging from quasi-static to dynamic stretching, this study developed a synchronized electromechanical measurement system. This system facilitates simultaneous measurement of electrical and mechanical responses of the sensor at diverse loading rates. It can be categorized into two subsystems based on loading velocity: the quasi-static loading subsystem and the dynamic loading subsystem. The quasi-static trials are executed using a universal testing machine, whereas the dynamic experiments are carried out employing a Hopkinson bar. Further elaboration on these subsystems will be provided in the subsequent sections.

2.1. Loading subsystem

2.1.1. Quasi-static loading subsystem

The quasi-static loading subsystem, as illustrated in Figure 1, can be systematically divided into three primary components: the loading unit, the mechanical measurement unit, and the electrical measurement unit.

The loading unit (Figure 1(a)) is equipped with an Instron 5567 Universal Testing Machine (INSTRON, USA), which applies loading speeds ranging from 0.001 mm/min to 500 mm/min for specimens within the quasi-static tensile domain.

The mechanical measurement unit (Figure 1(b)) involves a comprehensive setup that includes a light source, an industrial camera (BFS-U3-31S4M-C, FLIR Systems Inc., USA), and a computer for controlling the camera. Given the insufficient accuracy of the displacement data from the testing machine, this research project further adopts DIC technology for a precise displacement measurement. The circuit diagram positioned in the lower right corner of the figure illustrates the integration of the power supply, reference resistor, and electrical signal acquisition channel into the universal testing machine.

The electrical measurement unit (Figure 1(c)) employs a voltage divider circuit, with data acquisition facilitated through a dedicated electrical signal acquisition channel integrated within the universal testing machine. The direct current power supply utilizes the UTP 1310 model (Uni-Trend Tech. Co. Ltd., China).

2.1.2. Dynamic loading subsystem

Figure 1
The quasi-static loading subsystem comprises three main components: (a) the loading unit, (b) the mechanical measurement unit, and (c) the electrical measurement unit

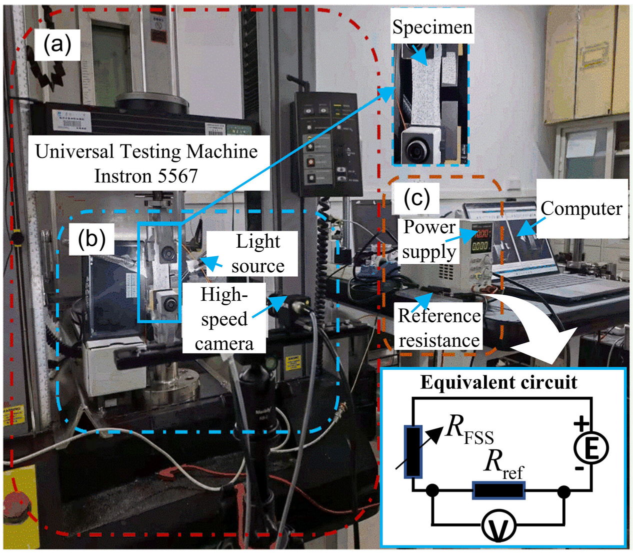

Figure 2
Dynamic loading subsystem: (a) the schematic diagram of the dynamic loading subsystem and (b) picture of the subsystem with illustrations

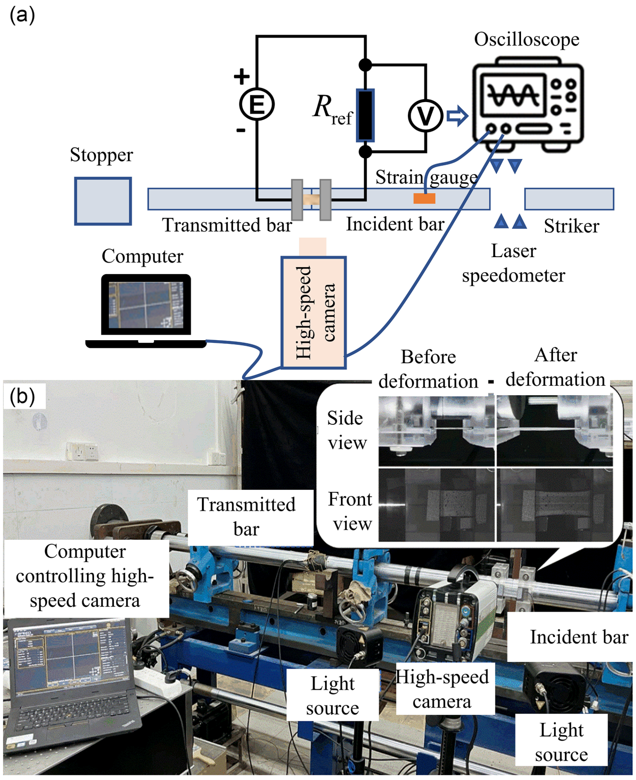

Figure 2 illustrates the dynamic loading subsystem. The loading unit is a critical component, and it comprises a SHPB and a specially designed fixture. The SHPB's transmission rod facilitates the rapid displacement of one end of the specimen, enabling dynamic tensile loading over time. The specimen is securely fastened to the rod via the fixture, which retains both ends of the specimen on the incident and transmission rods of the SHPB. This configuration allows dynamic loading to both ends of the specimen simultaneously.

The system incorporates both electrical and mechanical measurement units. The former is configured using a voltage divider circuit, where real-time voltage measurements of the reference resistor are captured using the DSOX4024A oscilloscope (Keysight Technologies Inc., China) to compute real-time resistance variations of the sensor. The latter employs DIC technology, with the i-speed726 high-speed camera (iX camera, UK) utilized for image acquisition under computer control.

Regarding the optimal positioning of the high-speed camera and light sources, the setup ensures accurate data acquisition. A black cloth served as the experimental backdrop, and two high-intensity light sources were strategically positioned to illuminate the specimen, enhancing the exposure. The distance between the camera and the specimen was approximately 200 mm, and prior to the experiment, the camera's optical axis was calibrated to be perpendicular to the surface of the FSS using a mirror and laser. Once the positions of the high-speed camera (IX i-speed726) and the intense light sources were established, the high-speed camera was connected to the control computer.

During the experiment, the strain gauge attached to the incident bar was utilized to trigger the simultaneous switching of mechanical and electrical acquisition systems, thereby achieving synchronous signal acquisition. The FSS was captured from both frontal and top-down viewpoints, with the top-down view ensuring that the FSS experienced no torsion during the test. This setup ensures accurate and reliable data acquisition for dynamic loading experiments.

2.2. Key features of the measurement system

2.2.1. High accuracy

In this study, the experimental setup for assessing the electrical performance of the sensor was streamlined by employing a voltage divider circuit. Consequently, the experimental apparatus comprises only a power supply, wires, a reference resistor, and an electrical signal acquisition device.

The power supply (UTP 1310) has a supply error not exceeding 0.1%. The oscilloscope employed is the InfiniiVision DSOX4024A, produced by KEYSIGHT. The reference resistor exhibits a resistance deviation of less than 0.1% relative to its nominal value. The wires used in the experiment are XBGD (Xinghai Co. Ltd., China) 1.2 mm^2 pure copper flexible test wires, capable of handling a maximum current of 6 A and withstanding a voltage of 3 000 V. The resistance of these wires is less than 0.01 ‰ of the sensor resistance, rendering wire resistance negligible.

During the measurement, the resistance value of the reference resistor must be optimized based on the resistance range of the sensor. This optimization seeks to determine a reference resistor value that maximizes the variation in the measured reference resistance during the experiment while simultaneously minimizing the discrepancy between the measured sensor resistance and its true value.

Based on multimeter measurements, the FSS exhibited an initial resistance ($R_{\mathrm{FSS\_initial}}$) of 58 kΩ, which increased to 400 kΩ ($R_{\mathrm{FSS\_strained}}$) under 100% strain. For computational purposes, the resistance variation range of the sensor was defined as 50 kΩ ($R_{\mathrm{FSS\_min}}$, a practical adjustment from the initial value) to 400 kΩ ($R_{\mathrm{FSS\_max}}$), with an optimal reference resistor value ($R_{\mathrm{ref\_opt}}$) calculation range set at 0 kΩ to 200 kΩ. Assuming a constant power supply voltage (E) of 10 V, the study aims to determine the $R_{\mathrm{ref\_opt}}$ that maximizes the variation in measured voltage (V) relative to changes in sensor resistance (R_{FSS}). To achieve this, the relationship between V and R_{FSS} was established, as depicted in Equation (1). The parameter utilized for optimal selection of the reference resistance is listed in Table 1.

Table 1
Parameters for optimal selection of the reference resistance

Parameter	Value
Supply voltage (V)	10
R_{FSS} (kΩ)	[50:10:400]
R_{ref} (kΩ)	[0:5:1000]

$$V = \frac{E}{R_{\mathrm{ref}} + R_{\mathrm{FSS}}} \times R_{\mathrm{ref}} \tag{1}$$

MATLAB simulation revealed that, for a fixed R_{ref}, V increased with rising R_{FSS}, as illustrated in Figure 3(a). Notably, when R_{ref} was set to 115 kΩ, the range of V variation is maximized, as shown in Figure 3(b), yielding optimal experimental outcomes. Consequently, 115 kΩ was identified as the $R_{\mathrm{ref\_opt}}$. It is imperative to reselect the reference resistor based on the specific conditions of each sensor specimen prior to experimentation to ensure accuracy.

In the present study, the resistance changes of the FSSs are measured using a voltage-dividing circuit. The UT39E+ digital

Figure 3
(a) Range of the measured voltage caused by FSS stretching with a reference resistance of 115 kΩ and (b) change range of the measured voltage with the reference resistance

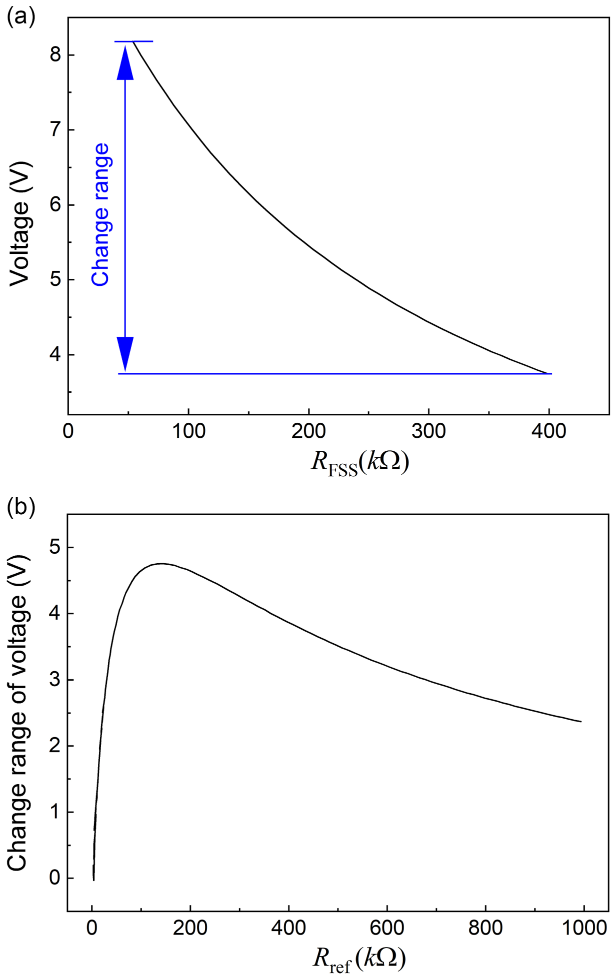

multimeter (Uni-Trend Tech. Co. Ltd., China) served as the reference instrument. Its measurement accuracy is 0.3% for the 2 kΩ to 2 MΩ range. During the dynamic stretching process, an oscilloscope is used for recording. After optimizing the reference resistance in the voltage-dividing circuit, the maximum measurement deviation is 2% due to the environmental noise. Since we are considering the relative resistance change here, the proposed electrical signal measurement device in this research achieved an average measurement accuracy of 0.47% and incorporated a feature that enables the adjustment of the reference according to the resistance range under measurement. As a result, the measurement accuracy of this device remains uniform across all measurement ranges. Therefore, the proposed electrical signal measurement device consistently maintains a high overall measurement accuracy and, within certain measurement ranges, surpasses the accuracy levels of conventional acquisition devices.

2.2.2. Constant high-speed loading over large deformation

The SHPB, traditionally employed as both a loading and a measurement device in dynamic tension-force and electrical synchronous measurement systems, functioned solely as a loading device in this study. Unlike alternative dynamic loading methods, such as drop hammer or explosive loading, the Hopkinson pressure bar's loading speed can be precisely controlled by adjusting the air pump's released pressure. This feature ensures greater control over the Hopkinson pressure bar's dynamic acceleration. Furthermore, the incorporation of lubricating oil and ball-bearing devices between the support and rod components effectively minimizes frictional forces in the loading direction. This design significantly extends the duration of the bar's constant velocity loading stage, thereby providing an extended period of high-speed, uniform tensile loading for the specimen. It is worth noting that the SHPB utilized in this study accelerates the projectile via air pressure impact, enabling the generation of high acceleration within a short timeframe.

Figure 4 illustrates the loading velocity and corresponding sensor strain during a dynamic tensile test. It reveals that the device accelerated to approximately 0.55 m/s within 0.003 s and maintained a constant velocity loading phase for 0.063 s, accounting for roughly half of the total loading time. During this phase, sensor strain increased from 2.84% to 72%, encompassing the strain range of interest (5% – 60%). The loading system's capability to rapidly achieve and sustain constant velocity loading over an extended duration makes it suitable for large deformation dynamic tensile loading applications, as evidenced by the sensors' uniform velocity stretching within the 0.03 – 0.72 strain range, indicating the system's capacity to provide sustained uniform stretching for the specimens.

Figure 4
Loading velocity versus strain during dynamic loading

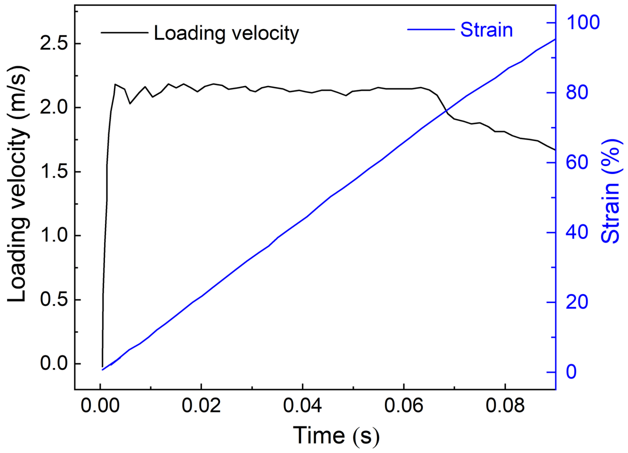

The SHPB's bullet, incident rod, and transmission rod must be constructed from the same material, positioned horizontally and coaxially, and possess identical diameters. Typically, the bar employs materials characterized by high strength and toughness, such as high-strength steel and alloy steel. This design enables the SHPB to withstand substantial dynamic loads and transmit velocities at high rates. In the experiment, the specimens were secured between the incident rod and transmission rod, with the transmission rod's maximum displacement exceeding 300 mm. This configuration facilitated the stretching of the FSS to over 600% strain, fully satisfying the requirements for large deformation tensile testing of flexible conductive materials.

2.2.3. Wide range of loading rates

In the SHPB system, the bullet's launch velocity is proportional to the applied launch air pressure, enabling precise control over the bullet's velocity to align with the specific speed requirements of various impact experiments. The SHPB employed in this investigation comprised alloy steel rods with a diameter of 75 mm, while the bullets utilized were 600-mm-long steel rods. The material and geometric specifications of the SHPB are detailed in Table 2. Theoretically, it can generate a launch air pressure of approximately 1 MPa, which translates to a theoretical bullet velocity range spanning from 5 m/s to 20 m/s. During trials, the maximum achievable launch air pressure was approximately 0.6 MPa, yielding a corresponding maximum bullet velocity of around 16 m/s. Both the launch air pressure and the bullet velocity were monitored using a velocity gauge integrated into the SHPB setup. Typically, upon bullet launch, the velocity gauge captures the bullet's speed as it traverses the gauge and presents this data in a digital format. To elucidate the correlation between launch air pressure and bullet velocity, a series of measurements were conducted at varying launch air pressures, with the results illustrated in Figure 5.

Prior to conducting the experiment, the incident bar and the transmission bar were initially in contact, with the bullet transferring its kinetic energy to both bars upon collision. Given the incorporation of a ball-bearing mechanism and an adequate supply of lubricating oil between the bar rods and their supports, it is reasonable to assume that the effects of friction are minimal in the experiment, and as such, friction is disregarded in the analysis. When a bullet strikes the incident bar, both the bullet

Table 2
Parameters of SHPB made from alloy steel

Parameter	Value
Density (kg·m^{-3})	7800
Elastic modulus (GPa)	210
Poisson's ratio	0.25
Sound velocity (m·s^{-1})	5200
Diameter of bars (mm)	74
Length of striker (mm)	600
Length of incident bar (mm)	3000
Length of transmitted bar (mm)	2000
Emission pressure (MPa)	0.02~1.00

Figure 5
The relationship between the projectile velocity and the air pressure

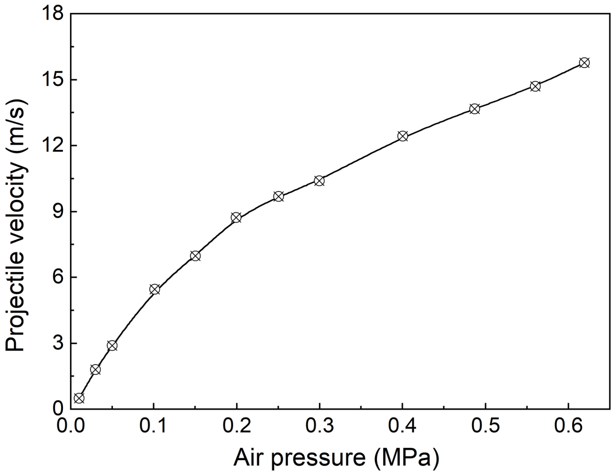

Figure 6
Time-loading velocity and time-strain curves during loadings at (a) 1.0 m/s, (b) 2.1 m/s, and (c) 3.7 m/s

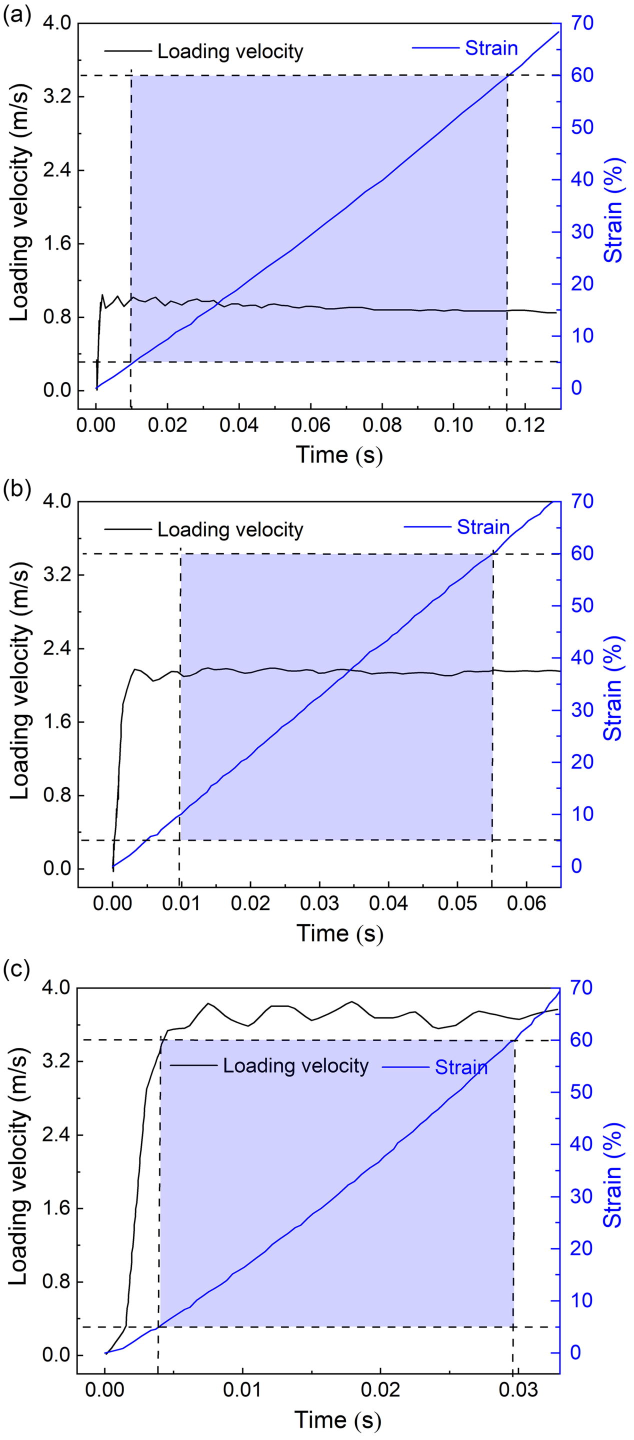

and the incident bar come to a halt, transferring all their kinetic energy to the transmission bar. This causes the transmission bar to move, with its velocity representing the loading velocity applied to the experimental specimen. Calculations show that the Hopkinson bar can theoretically provide loading velocities ranging from 1.2 m/s to 6 m/s, allowing for strain rates ranging from 20 s^{-1} to 120 s^{-1} to the resistive FSS specimens used in this study.

Figure 6 illustrates the time, loading velocity, and strain curves for various loading rate experiments. During the tensile process, all experiments with different loading rates exhibited a rapid acceleration phase followed by a prolonged period of constant loading velocity, known as the steady-state or uniform loading phase. This uniform loading phase was maintained within the strain range of 5% to 60% for all loading rates. By integrating the loading units from both the quasi-static and dynamic tensile-electrical measurement systems, the proposed flexible conductive material tensile-electrical measurement system in this study enables synchronized force-electrical signal measurement at loading speeds ranging from 1×10^{-3} mm/min to 3.7×10^{5} mm/min. This system facilitates the application of various loading rates to flexible conductive materials. In daily activities and fitness routines, human movement velocities are typically below 10 m/s, while athletes may reach speeds of approximately 30 m/s [18]. The experimental speed range of this system covers most of the movement velocities encountered in everyday life. For higher-speed loading experiments, adjustments can be made to the dimensions of the Hopkinson pressure bar components, thereby meeting the requirements for higher-speed experimental loading.

2.3. Specimens

2.3.1. Configuration of FSSs

The fabric-based strain sensor comprised three components: a conductive film, an elastic fabric substrate, and woven fabrics. The conductive film was formulated by dispersing carbon nanoparticles (CNPs) within an elastic composite matrix composed of silicon elastomer (SE) and silicon oil, as detailed in Wang et al. [26]. Scanning electron microscopy analysis reveals a rough surface morphology for the fabric-based strain sensor, characterized by uniform distribution of CNPs throughout the SE matrix, as documented in Chen et al. [27]. The conductive film was screen-printed onto the fabric substrate, after which a layer of silicone gel was applied to encapsulate the conductive film, thereby ensuring electrical insulation.

The polyurethane (PU) yarn employed in the knitted fabric substrate exhibited a low modulus and a high elasticity, and the yarn was incorporated into the fabric structure along the wale direction [10], which allow the substrate fabric to endure stretching beyond 200%. Further, to minimize the exposed area of the PU yarn, it was enveloped with polyamide (PA). The double-layered PA envelope on the PU yarn substantially improves the transverse stability of the fabric, while the elastic yarn accommodates deformation along the stretching direction. This configuration enhances the overall elastic modulus of the fabric substrate and facilitates the sliding of yarn intersections during stretching, thereby effectively mitigating mechanical hysteresis within the fabric substrate [28].

The FSS employed in this study was designed as a π-shaped configuration, enabling the conductive terminal to be positioned on one side of the sensor, thereby facilitating wire connection during practical applications. The thickness of the conductive film and silicone encapsulation layer within the sensor measured 0.494 ± 0.005 mm, with an overall mass of 997.8 ± 35.7 mg. The active stretching area of the sensor comprised two identical rectangular conductive films (illustrated in Figure 7), each measuring 8.0 mm in width and 48.5 mm in length. The non-stretching region of the FSS was defined by the woven fabrics on its rear side. Given the FSS's low elastic modulus, it is prone to deformation during mounting. To maintain the sensor's stability during non-operational periods, it must be secured using a C-shaped cardboard support. It is imperative to note that the sensor should remain undisturbed for a minimum of 24 h post-experiment to ensure complete recovery to its original state following stretching.

2.3.2. Preprocessing of FSSs

The conductive composite film and the fabric substrate are different in elastic modulus. Therefore, cracks can be generated in the conductive film of the sensor during stretching, resulting in a permanent increase in its electrical resistance [29]. Therefore, it is necessary to stabilize the sensor by three cycles of 100% strain pre-stretching. Furthermore, to facilitate the analysis of the strain distribution of FSS during high-speed stretching, specimens must undergo speckle treatment prior to experimentation. This process entails spraying black paint on the white side of FSS (the backside of the knitted fabric substrate) to generate speckle patterns. Comparing experimental data at identical stretching rates before and after speckle treatment (illustrated in Figure 8) reveals that the sensor specimens' sensitivity coefficient was approximately 4.9 pre-treatment and 4.8 post-treatment. While loading phase performance remained largely unchanged post-treatment, the unloading phase was impacted, leading to reduced hysteresis during cyclic stretching. Additionally, the applied speckles' diameter, ranging from 0.5 to 3 mm and differing by an order of magnitude from the specimen size, enables measurement of the continuous strain field in fabric sensors.

Figure 7
The configuration of FSS: (a) schematic of FSS from an oblique view, (b) schematic of sensor from a front view, (c) definition of stretching and non-stretching area, and (d) a picture of the FSS on cardboard support in black color

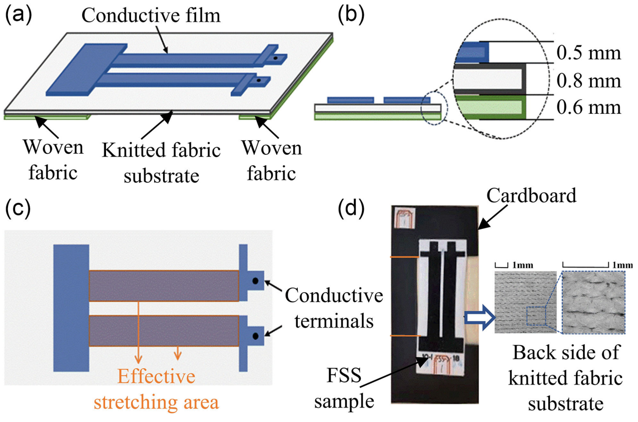

Figure 8
Strain-resistance curves of FSS before and after spraying speckles

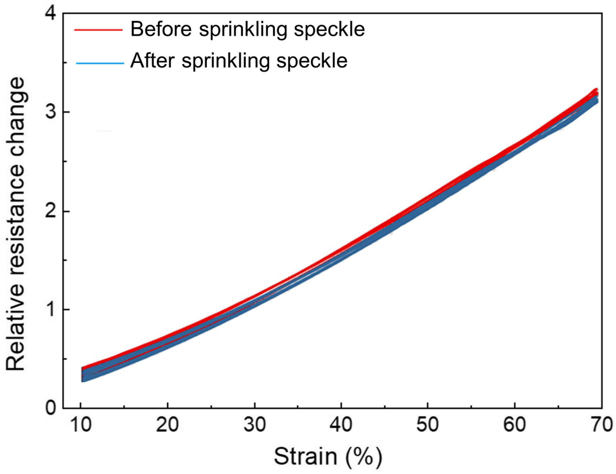

2.4. More experimental setup

The quasi-static measurement system utilized a universal testing machine to perform tensile tests on frequency-selective surface specimens. Initially, the sensor specimen was mounted along with the electrical signal transmission device onto the testing machine, ensuring that the sensor remained in a uniaxial tensile state throughout the experiment for accurate measurement. After securing the specimen, the optimal reference resistance value was determined based on its initial resistance, and the specimen was connected to the electrical signal measurement unit.

Next, the DIC system was configured. A small display screen was placed behind the specimen to indicate the experiment start time, facilitating alignment and calibration of the displacement data from the universal testing machine. Light sources were positioned on either side of the sensor specimen to improve illumination. The camera was then aligned directly in front of the sensor specimen, ensuring that its optical axis is perpendicular to the specimen surface and that the field of view includes the display screen, the entire specimen, and the speckle pattern used for computing tensile displacement. The resulting images are illustrated in Figure 9.

For the detection of displacement in dynamic stretching experiments utilizing DIC techniques, pre-fabricated speckle stickers were separately adhered to two fixtures (as depicted in Figure 2). The displacement of each fixture was acquired through DIC. Subsequently, the disparity in displacement between the two fixtures was computed using Equation (2), thereby enabling the determination of the loading displacement (U) on the FSS during the stretching process.

$$U(t) = U_t(t) - U_i(t) \tag{2}$$

where $U_t(t)$ and $U_i(t)$ represent the real-time displacements of the transmitted bar and incident bar, respectively. The loading rate during the experiment was then calculated using Equation (3):

Figure 9
Typical images from high-speed camera for DIC displacement measurement: (a) quasi-static measurement, and (b) dynamic measurement

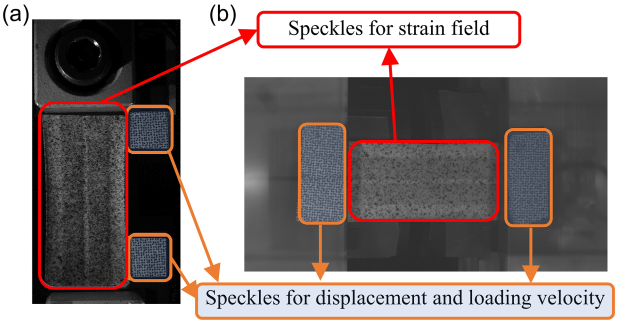

$$v(t) = \frac{U(t + \Delta t) - U(t)}{\Delta t} \tag{3}$$

The primary component of the dynamic measurement system is the Hopkinson bar. Prior to specimen installation, fixtures must be secured to the incident and transmitted bars. To prevent slippage (relative displacement) between the specimen, fixtures, and Hopkinson bar, a 0.3 mm silicone gel layer should be applied between the fixtures and the Hopkinson bar, with bolts tightened firmly.

Next, connect the electrical signal measurement circuit as in Figure 2, and configure the oscilloscope's display range and acquisition frequency according to experimental specifications. Ensure the entire tensile process is recorded by setting the oscilloscope to capture electrical signals at the highest possible frequency. Implement automatic falling-edge trigger conditions and adjust the trigger level to an appropriate voltage.

For optical clarity, employ black cloth as the experimental backdrop and position two high-intensity light sources to illuminate the specimen. Position the camera approximately 200 mm from the specimen and align its optical axis perpendicular to the FSS surface using a mirror and laser. Once the high-speed camera (IX i-speed726) and light sources are positioned, connect the camera to the control computer for image storage. Besides, to maintain image clarity, maximize the shooting frequency while keeping the resolution within the minimum range necessary to document the full experiment. In this study, the camera resolution was set to 2048 × 800 pixels (Horizontal × Vertical), with a frame rate of 10000 Hz. The corresponding horizontal shooting range is approximately 250 mm. The spatial accuracy is approximately 0.01 mm since DIC can obtain the changes in 0.1 pixel. Moreover, to solve the problem of system synchronization, the same trigger signal is used for displacement measurement and voltage measurement.

Upon initiating the Hopkinson bar, the bullet was propelled by the air pump, striking the incident and transmitted bars, inducing high-speed displacement in the transmitted bar and stretching the specimen. During the experiment, the oscilloscope and high-speed camera triggered automatically and performed synchronous measurements using the signal from the Hopkinson bar's strain gauge.

3. Results and Discussion

3.1. Experimental curves

To measure the electromechanical performance of the sensor during high-speed stretching and investigate the relationship between force-electric signal and strain rate, the sensor's ends were secured to the incident and transmitted bars of a Hopkinson bar, subjecting it to high-speed tensile loading. A total of 48 experiments were conducted on six FSS specimens. After each experiment, the sensor rested for at least 24 h to restore to its initial state before the next test. For the initial experiment of each sensor, a cyclic stretching test was performed ten times using a tensile testing machine to assess the repeatability of each FSS. A sensor specimen with sufficient repeatability was selected for subsequent experiments.

During data processing, measured resistance signals were normalized to mitigate experimental errors due to initial resistance variations. The relative resistance change, R_r (Equation (4)), was calculated as follows:

$$R_r = \frac{R - R_0}{R_0} \tag{4}$$

where R represents the measured resistance of the sensor, and R_0 denotes the initial resistance of the sensor before the experiment.

Quasi-static tensile experiments on FSSs were conducted using an Instron 5567 electronic materials testing machine. The FSSs described in Section 3.1 were employed, with loading speeds set at 10, 150, 300, 400, and 500 mm/min. Sensors underwent ten cyclic stretches from 5% to 60% strain by controlling applied displacement. Both electrical and mechanical signals were recorded by the Instron. Displacement signals were obtained and optimized using DIC techniques. The nominal strain during loading was calculated from corrected displacement data:

$$\varepsilon(t) = \frac{U(t)}{l_0} \tag{5}$$

where U represents the vertical displacement (applied tensile displacement in mm). l_0 denotes the length of the sensing region of the sensor, which is the effective gauge length. In this study, the average effective gauge length of the sensors used was 48.68 mm.

Experimental data are illustrated in Figure 10. Displacement data were used to calculate strain of FSS (Figure 10(a)). Measured voltage data were employed to determine relative resistance during stretching (Figure 10(b)). Strain and resistance data were plotted to generate the strain-resistance curve for the ten-cycle experiment (Figure 10(c)), revealing patterns in the sensor's strain-resistance relationship during stretching. It is evident that the FSS demonstrates excellent repeatability in strain and relative resistance change across 10 cycles of tensile stretching, with no discernible attenuation phenomenon observed.

Dynamic tensile experiments were performed using the SHPB to apply tension to one end of the test specimen. Throughout the stretching process, high-speed cameras captured sequential images, which were subsequently processed using DIC software. The software analyzed the speckle patterns in the images to compute the displacement difference between the two fixtures, thereby determining the loading displacement of the specimen during the experiment.

Based on the loading displacement data, the nominal strain of the FSS was calculated, yielding the strain curve of the specimen over the entire loading duration, as illustrated in Figure 11(a). Furthermore, voltage data acquired during the experiment were employed to compute the relative resistance change of the sensor, with results presented in Figure 11(b). Finally, the calculated strain and resistance data were utilized to construct the strain-resistance curve, as depicted in Figure 11(c).

Figure 10
Electromechanical signals from the FSS during quasi-static tensile tests: (a) strain-time curves, (b) relative resistance change-time curves, and (c) strain-resistance curves

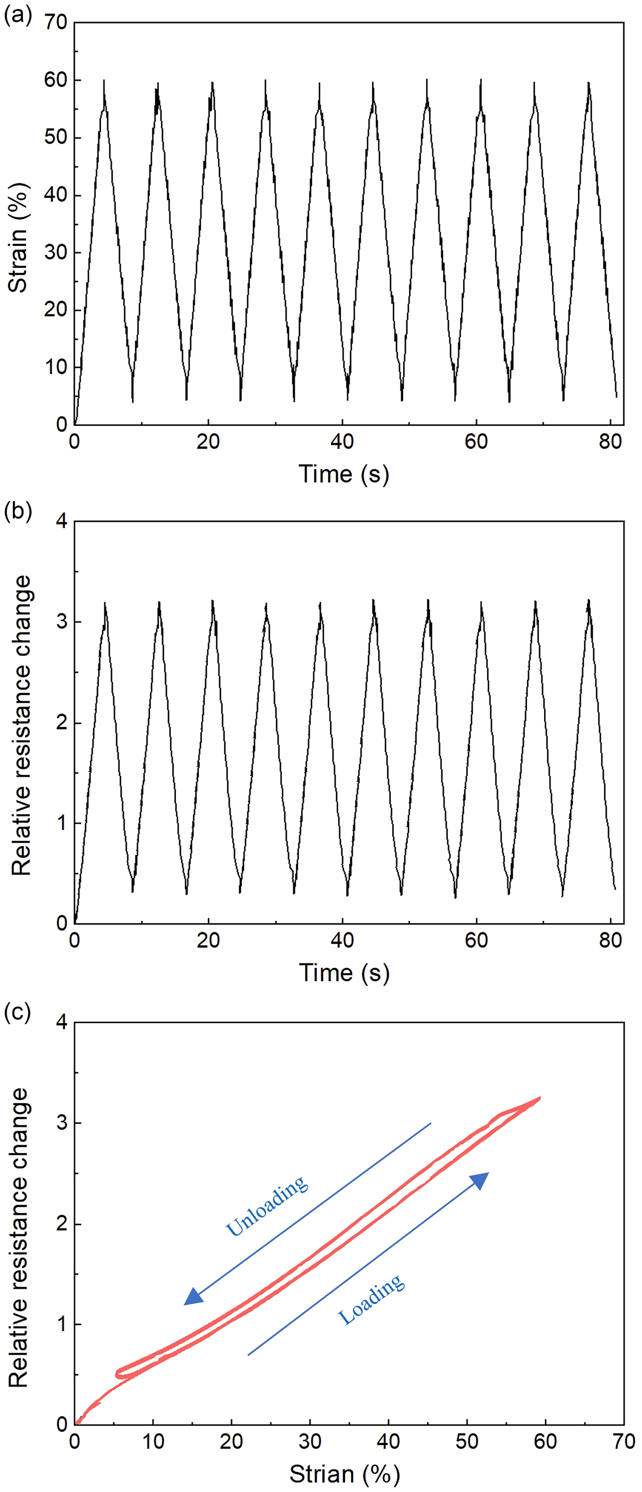

Figure 11
Electromechanical signals from the FSS during dynamic loading: (a) strain-time curves, (b) relative resistance change-time curves, and (c) strain-resistance curves

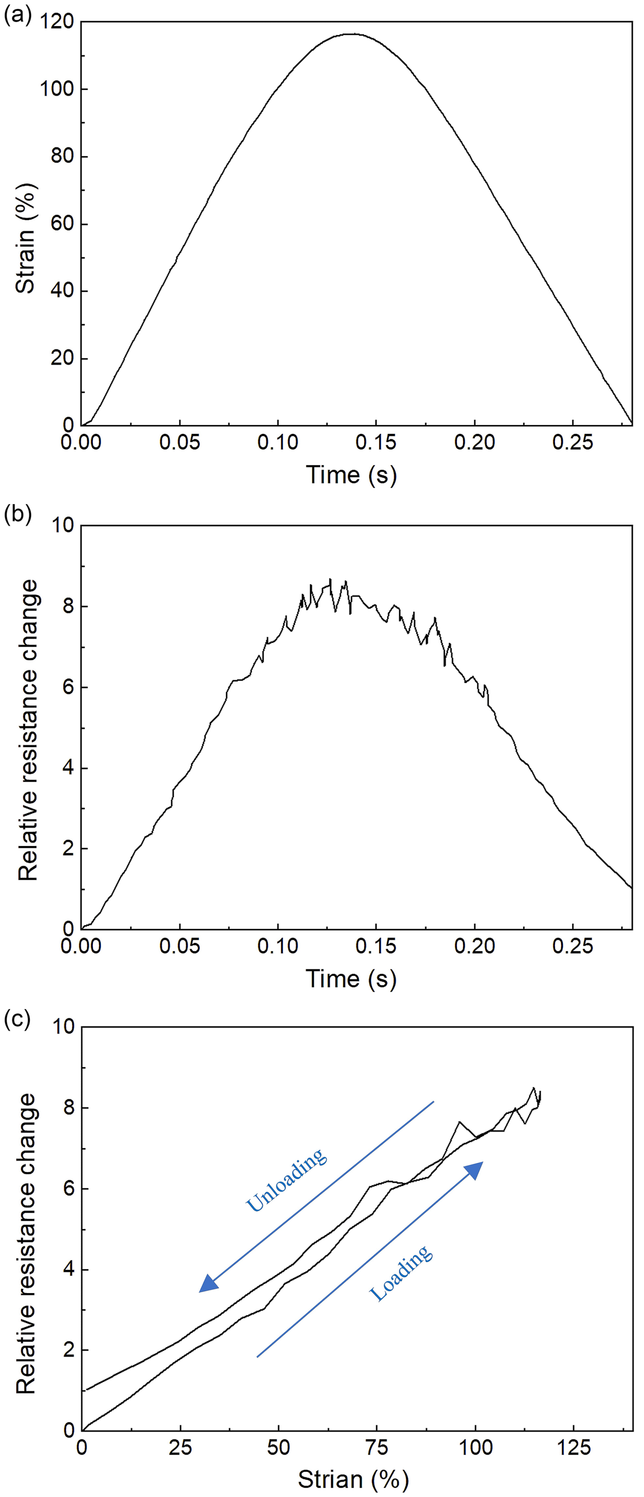

3.2. Variation of sensitivity with strain rate

The sensitivity coefficient, which is also termed as gauge factor [26], is defined as a crucial metric for assessing the amplification level of the sensor's response to the input stimulus. In the context of fabric-based strain sensors, the sensitivity coefficient correlates with the measured strain and relative resistance values during tensile testing.

In the application of human motion capture, the sensors shall undergo tensile deformation within the strain rate range of 0.01 s^{-1} to 20 s^{-1}, which is calculated according to the speed range given in Buddhadev and Martin [15], Law and Li [16], Beránek et al. [17],

Figure 12
Electromechanical properties of FSS influenced by strain rate

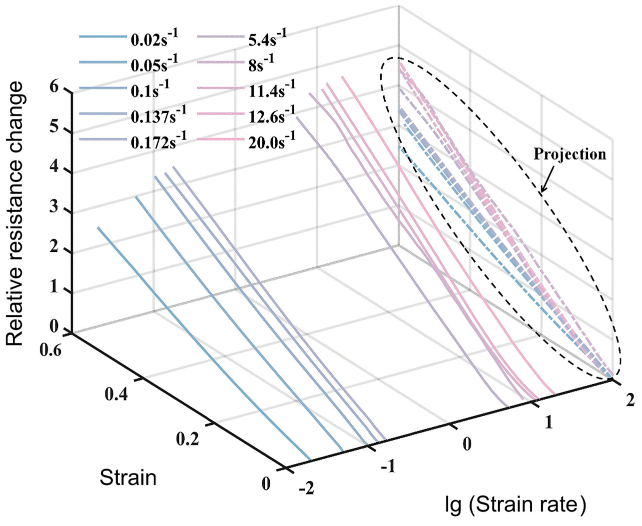

and Cao et al. [18]. By analyzing the strain-relative resistance curves for each experimental run, the sensor specimens' strain-relative resistance behavior was plotted against strain rate, as illustrated in Figure 12.

On one hand, the slopes of these curves, which are namely the gauge factors of the strain sensors, exhibited variations with increasing strain rates, showing an upward trend with higher loading rates. In order to better show the changes in gauge factors, the solid lines have been projected to the plane of strain and relative resistance change. This trend is well consistent with results from Wang et al. [20], although that paper included only two strain rate levels, 0.4/s and 50/s. Nonetheless, the strain-relative resistance variation curves retained an approximately linear relationship throughout the loading process across different strain rates. On the other hand, the theoretical model between strain rate and the sensitivity of resistive fabric sensors as established in Wang et al. [20] also confirmed the above trend, and there was an exponential relationship between sensitivity and strain rate. Therefore, the changes in strain rate have a quite significant effect on sensitivity of the sensors, and in real application involving dynamic conditions, the strain rate needs to be considered when calculating the nominal strain. That is also why we need to logarithm the strain rate when plotting Figure 12.

Fortunately, despite the noticeable strain rate effect, it is evident that the strain and relative resistance of the textile-based strain sensor remained approximately linear during stretching at varying rates, as can be seen in Figure 10. To derive an empirical formula for the sensor's force-electrical performance relative to strain rate, a linear function was employed to model the strain-relative resistance behavior of the specimen during the stretching process, as follows:

$$R_r = k\varepsilon \tag{6}$$

where ε denotes the nominal strain, k is the sensitivity coefficient related to the loading strain rate.

3.3. Variation of strain field with strain rate

The fabric surface was comprised of numerous knitted loops, each representing a simplified unit. These loops were interconnected in series and parallel configurations, forming a knitting unit network, as depicted in Figure 13 [30]. During stretching, a strain gradient distribution became apparent, with higher strains observed at the edge regions of these unit grids. As the strain intensifies, the strain level disparities within each unit grid become increasingly pronounced.

Figure 13
(a) Knitted structure of fabrics and simplified cell network and (b) an optical image of the substrate fabric (1.3 mm × 1.3 mm)

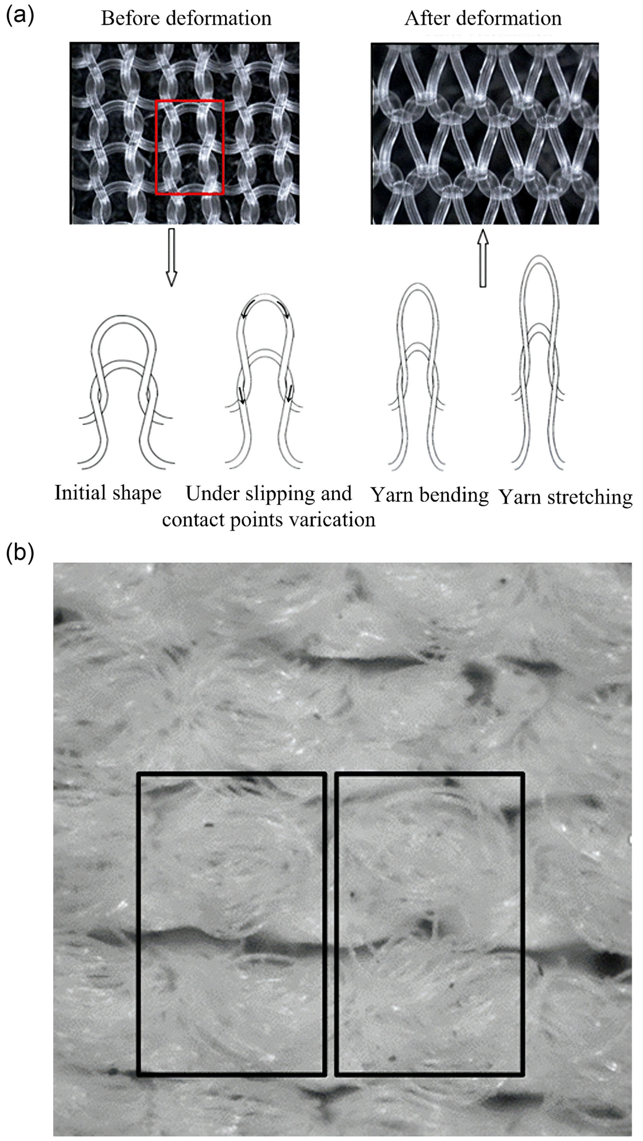

This study further conducted a more in-depth analysis of the strain distribution in FSS under dynamic tensile loading. Figure 14 displays real-time strain field contour maps of an identical specimen subjected to tensile loading transitions from quasi-static to dynamic conditions at equivalent strain levels. The left-hand side of the sensor depicted in the figure corresponds to the fixed end of the tensile test setup, whereas the right-hand side signifies the stretching end. Within the quasi-static loading range (with a loading rate of 0.05 s^{-1}), the real-time strain field configurations at various strain levels exhibited similarity but were irregular in shape. Multiple tests conducted on the same specimen revealed that areas of higher strain within the real-time strain field maintained consistency during low-speed stretching at different rates. This phenomenon has previously been reported in

Figure 14
Contour map of sensor deformation field during tensile tests at different strains and strain rates

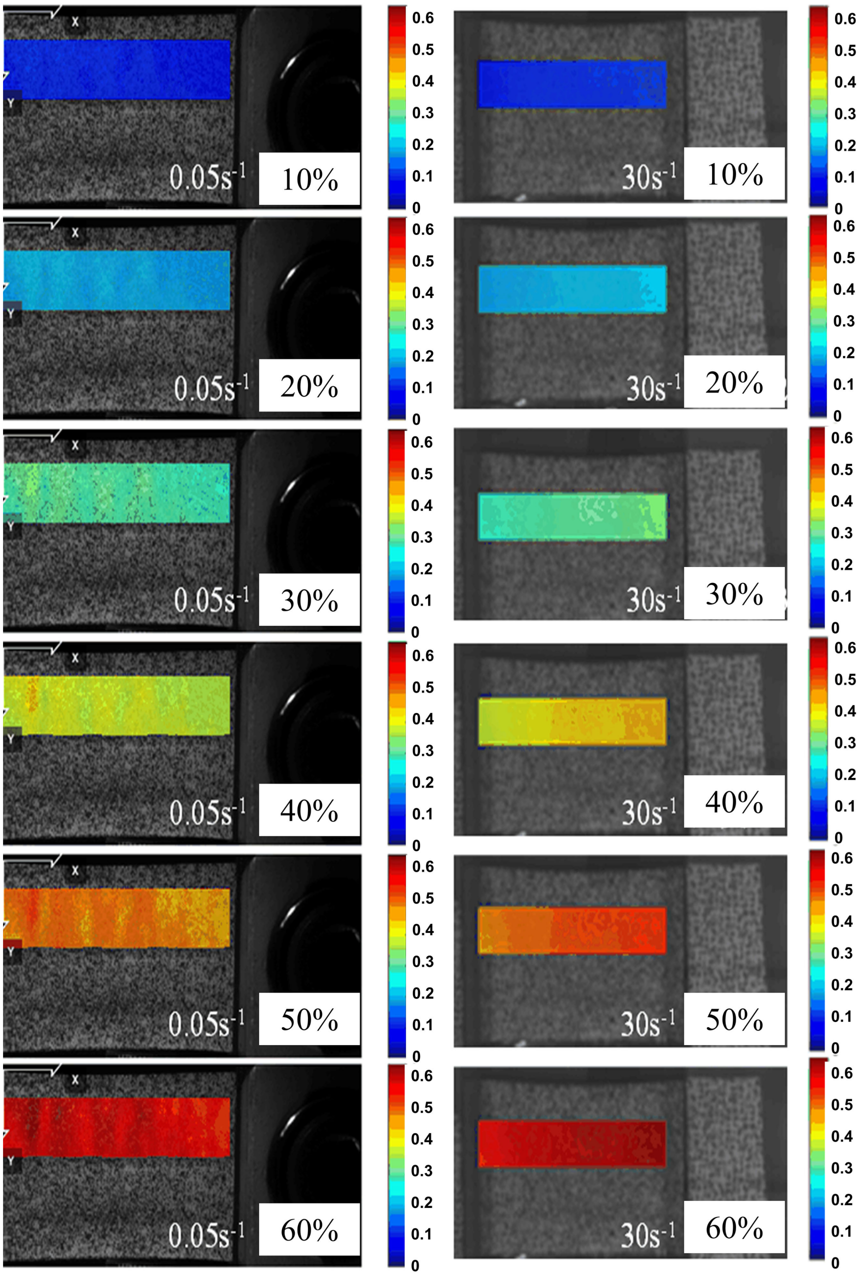

printed fabric sensors [26], where the sensors are claimed to exhibit grid patterns associated with the interaction between the screen-printing process and the fabric structure. In contrast, when the loading rate fell within the dynamic tensile range (at a loading rate of 30 s^{-1}), a pronounced gradient trend became evident in the strain field distribution of the sensor.

4. Conclusion

In this research, by developing an experimental system tailored for synchronized dynamic force-electrical measurement under large deformation, we enabled the simultaneous acquisition of mechanical and electrical signals from FSS during stretching at varying strain rates. This capability has facilitated a comprehensive investigation into the interplay between mechanical and electrical properties during deformation, revealing that the correlation between these signals is highly dependent on the strain rate. Furthermore, the application of DIC method has allowed us to calculate the deformation field of FSS at various tensile strain rates and analyze the intricate relationships between the strain field, tensile strain, and strain rate. Our findings underscore the strain rate sensitivity of FSS, demonstrating that the slope of the strain-relative resistance curve increases with strain rate, yet maintaining an approximately linear relationship during uniform loading at different tensile rates. Additionally, strain field analysis revealed that quasi-static low-speed stretching leads to larger local strains in weak manufacturing positions or structural cell positions, whereas dynamic high-speed stretching produces a more regular strain field pattern with larger local strains in the stretching section and minimal local strains at the fixed end. These insights contribute significantly to the optimization and design of FSS for various applications.

It is admitted that this study has two major limitations. The FSS's performance during unloading is unstable; hence, the research does not include mechanical and electrical properties during unloading. Additionally, the influence of external conditions such as temperature and humidity on sensor performance requires further investigation.

Recommendations

This research aims to address the critical gaps in understanding the performance of fabric-based strain sensors (FSSs) under large deformations and varying loading rates, offering novel methodologies to advance this field. We developed a synchronized measurement system that combines mechanically controlled loading, voltage divider circuits, and visual measurement technologies. This system enables a synchronized electromechanical assessment of FSSs under large deformations, covering a wide range of loading conditions from quasi-static to high-speed. We implemented precisely controlled loading rates during large deformations and accurately recorded the electromechanical behaviors of the sensors. Moreover, we analyzed the sensitivity characteristics and strain field distributions of FSSs under high-speed tensile deformation. Therefore, these findings can be a powerful tool to study the dynamic performance of soft strain sensors.

Funding Support

This work was supported by the Guangdong Provincial Natural Science Foundation (Grant No. 2024A1515011076, 2025A1515011999, and 2023A1515012942) and the National Natural Science Foundation of China (Grant No. 12472179, 12432008, 12472180, and 12372181). Fei Wang would like to acknowledge the support from Wuyi University for the "High-level Talent Start-up Scheme" (Grant No. 2021AL034).

Conflicts of Interest

The authors declare that they have no conflicts of interest to this work.

Data Availability Statement

Data are available on request from the corresponding author upon reasonable request.

Author Contribution Statement

Bao Yang: Conceptualization, Methodology, Formal analysis, Resources, Writing – original draft, Writing – review & editing, Supervision, Project administration, Funding acquisition. **Xianyu Zhu:** Software, Formal analysis, Data curation, Writing – original draft. **Chang Peng:** Software, Validation, Formal analysis, Investigation, Data curation, Visualization. **Licheng Zhou:** Conceptualization, Methodology, Resources, Writing – review & editing, Supervision, Funding acquisition. **Fei Wang:** Conceptualization, Methodology, Resources, Writing – original draft, Writing – review & editing, Supervision, Funding acquisition. **Zejia Liu:** Conceptualization, Methodology, Resources, Supervision, Project administration, Funding acquisition. **Liqun Tang:** Conceptualization, Methodology, Resources, Supervision, Funding acquisition. **Zhenyu Jiang:** Conceptualization, Methodology, Resources, Supervision, Funding acquisition. **Yiping Liu:** Conceptualization, Methodology, Resources, Supervision, Funding acquisition. **Senxin Chen:** Software, Validation, Investigation.

References

[1] Sun, F., Jiang, H., Wang, H., Zhong, Y., Xu, Y., Xing, Y., . . . , & Zhu, M. (2023). Soft fiber electronics based on semiconducting polymer. *Chemical Reviews*, *123*(8), 4693–4763. https://doi.org/10.1021/acs.chemrev.2c00720

[2] Niknejad, N., Ismail, W. B., Mardani, A., Liao, H., & Ghani, I. (2020). A comprehensive overview of smart wearables: The state of the art literature, recent advances, and future challenges. *Engineering Applications of Artificial Intelligence*, *90*, 103529. https://doi.org/10.1016/j.engappai.2020.103529

[3] Wang, J., Lu, C., & Zhang, K. (2020). Textile-based strain sensor for human motion detection. *Energy & Environmental Materials*, *3*(1), 80–100. https://doi.org/10.1002/eem2.12041

[4] Seyedin, S., Zhang, P., Naebe, M., Qin, S., Chen, J., Wang, X., & Razal, J. M. (2019). Textile strain sensors: A review of the fabrication technologies, performance evaluation and applications. *Materials Horizons*, *6*(2), 219–249. https://doi.org/10.1039/C8MH01062E

[5] Wang, X., Yu, H., Kold, S., Rahbek, O., & Bai, S. (2023). Wearable sensors for activity monitoring and motion control: A review. *Biomimetic Intelligence and Robotics*, *3*(1), 100089. https://doi.org/10.1016/j.birob.2023.100089

[6] He, X., Cai, J., Liu, M., Ni, X., Liu, W., Guo, H., . . . , & Qin, X. (2024). Multifunctional, wearable, and wireless sensing system via thermoelectric fabrics. *Engineering*, *35*, 158–167. https://doi.org/10.1016/j.eng.2023.05.026

[7] Zhang, J., Xu, B., Chen, K., Li, Y., Li, G., & Liu, Z. (2024). Revolutionizing digital healthcare networks with wearable strain sensors using sustainable fibers. *SusMat*, *4*(4), e207. https://doi.org/10.1002/sus2.207

[8] Lu, D., Chu, Y., Liao, S., Li, W., Cai, Y., Wei, Q., & Wang, Q. (2022). Highly sensitive fabric strain sensor with double-layer conductive networks for joint rehabilitation therapy. *Composites Science and Technology*, *230*, 109778. https://doi.org/10.1016/j.compscitech.2022.109778

[9] Rodgers, M. M., Alon, G., Pai, V. M., & Conroy, R. S. (2019). Wearable technologies for active living and rehabilitation: Current research challenges and future opportunities. *Journal of Rehabilitation and Assistive Technologies Engineering*, *6*, 2055668319839607. https://doi.org/10.1177/2055668319839607

[10] Xiong, J., Chen, J., & Lee, P. S. (2021). Functional fibers and fabrics for soft robotics, wearables, and human–robot interface. *Advanced Materials*, *33*(19), 2002640. https://doi.org/10.1002/adma.202002640

[11] Yin, R., Wang, D., Zhao, S., Lou, Z., & Shen, G. (2021). Wearable sensors-enabled human–machine interaction systems: From design to application. *Advanced Functional Materials*, *31*(11), 2008936. https://doi.org/10.1002/adfm.202008936

[12] Zhong, W., Ming, X., Li, W., Jia, K., Jiang, H., Ke, Y., . . . , & Wang, D. (2022). Wearable human-machine interaction device integrated by all-textile-based tactile sensors array via facile cross-stitch. *Sensors and Actuators A: Physical*, *333*, 113240. https://doi.org/10.1016/j.sna.2021.113240

[13] Gao, B., Jiang, J., Zhou, S., Li, J., Zhou, Q., & Li, X. (2024). Toward the next generation human–machine interaction: Headworn wearable devices. *Analytical Chemistry*, *96*(26), 10477–10487. https://doi.org/10.1021/acs.analchem.4c01190

[14] Jourdan, A., Rapacchi, S., Guye, M., Bendahan, D., Masson, C., & Bège, T. (2022). Dynamic-MRI quantification of abdominal wall motion and deformation during breathing and muscular

contraction. *Computer Methods and Programs in Biomedicine*, *217*, 106667. https://doi.org/10.1016/j.cmpb.2022.106667

[15] Buddhadev, H. H., & Martin, P. E. (2016). Effects of age and physical activity status on redistribution of joint work during walking. *Gait & Posture*, *50*, 131–136. https://doi.org/10.1016/j.gaitpost.2016.08.034

[16] Law, N.-Y., & Li, J. X. (2022). Biomechanics analysis of seven Tai Chi movements. *Sports Medicine and Health Science*, *4*(4), 245–252. https://doi.org/10.1016/j.smhs.2022.06.002

[17] Beránek, V., Votápek, P., & Stastny, P. (2023). Force and velocity of impact during upper limb strikes in combat sports: A systematic review and meta-analysis. *Sports Biomechanics*, *22*(8), 921–939. https://doi.org/10.1080/14763141.2020.1778075

[18] Cao, Y., Liu, Y., Tang, L., Jiang, Z., Liu, Z., Zhou, L., & Yang, B. (2024). Quantitative assessment of brain injury and concussion induced by an unintentional soccer ball impact. *Injury*, *55*(8), 111658. https://doi.org/10.1016/j.injury.2024.111658

[19] Wang, H., Hazell, P. J., Shankar, K., Morozov, E. V., Jovanoski, Z., Brown, A. D., . . . , & Escobedo-Diaz, J. P. (2020). Tensile properties of ultra-high-molecular-weight polyethylene single yarns at different strain rates. *Journal of Composite Materials*, *54*(11), 1453–1466. https://doi.org/10.1177/0021998319883416

[20] Wang, F., Zhu, B., Shu, L., Li, Y., Lai, X., Ma, L., . . . , & Tao, X. (2023). Smart clothing with built-in soft sensing network for measuring temporal and spatial distribution of pressure under impact scenarios. *Advanced Sensor Research*, *2*(2), 2200019. https://doi.org/10.1002/adsr.202200019

[21] Zhang, F., Hu, H., Hu, S., & Yue, J. (2021). Significant strain-rate dependence of sensing behavior in TiO_2@carbon fibre/PDMS composites for flexible strain sensors. *Journal of Advanced Ceramics*, *10*(6), 1350–1359. https://doi.org/10.1007/s40145-021-0509-7

[22] Brown, K. A., Brooks, R., & Warrior, N. A. (2010). The static and high strain rate behaviour of a commingled E-glass/polypropylene woven fabric composite. *Composites Science and Technology*, *70*(2), 272–283. https://doi.org/10.1016/j.compscitech.2009.10.018

[23] Todo, M., Takahashi, K., Béguelin, P., & Kausch, H. H. (2000). Strain-rate dependence of the tensile fracture behaviour of woven-cloth reinforced polyamide composites. *Composites Science and Technology*, *60*(5), 763–771. https://doi.org/10.1016/S0266-3538(99)00184-0

[24] Luo, Y., Abidian, M. R., Ahn, J.-H., Akinwande, D., Andrews, A. M., Antonietti, M., . . . , & Chen, X. (2023). Technology roadmap for flexible sensors. *ACS Nano*, *17*(6), 5211–5295. https://doi.org/10.1021/acsnano.2c12606

[25] Ates, H. C., Nguyen, P. Q., Gonzalez-Macia, L., Morales-Narváez, E., Güder, F., Collins, J. J., & Dincer, C. (2022). End-to-end design of wearable sensors. *Nature Reviews Materials*, *7*(11), 887–907. https://doi.org/10.1038/s41578-022-00460-x

[26] Wang, X., Yang, B., Li, Q., Wang, F., & Tao, X. (2021). Modeling the stress and resistance relaxation of conductive composites-coated fabric strain sensors. *Composites Science and Technology*, *204*, 108645. https://doi.org/10.1016/j.compscitech.2021.108645

[27] Chen, X., Wang, F., Shu, L., Tao, X., Wei, L., Xu, X., . . . , & Huang, G. (2022). A single-material-printed, low-cost design for a carbon-based fabric strain sensor. *Materials & Design*, *221*, 110926. https://doi.org/10.1016/j.matdes.2022.110926

[28] Li, Q., Wang, Y., Jiang, S., Li, T., Ding, X., Tao, X., & Wang, X. (2020). Investigation into tensile hysteresis of polyurethane-containing textile substrates for coated strain sensors. *Materials & Design*, *188*, 108451. https://doi.org/10.1016/j.matdes.2019.108451

[29] Yamaguchi, K., Busfield, J. J. C., & Thomas, A. G. (2003). Electrical and mechanical behavior of filled elastomers. I. The effect of strain. *Journal of Polymer Science Part B: Polymer Physics*, *41*(17), 2079–2089. https://doi.org/10.1002/polb.10571

[30] Wang, J. P., Xue, P., & Tao, X. M. (2011). Strain sensing behavior of electrically conductive fibers under large deformation. *Materials Science and Engineering: A*, *528*(6), 2863–2869. https://doi.org/10.1016/j.msea.2010.12.057

How to Cite: Yang, B., Zhu, X., Peng, C., Zhou, L., Wang, F., Liu, Z., . . . , & Chen, S. (2025). Synchronized Measurement of Electromechanical Responses of Fabric Strain Sensors Under Large Deformation. *Smart Wearable Technology*, 1, A7. https://doi.org/10.47852/bonviewSWT52026022